ROYAL SOCIETY OF CHEMISTRY

PAPER

Check for updates

Hydrogen bond-driven columnar self-assembly of electroluminescent D–A–D configured cyanopyridones†

D. R. Vinayakumara, [ID] [a] Hidayath Ulla, [ID] [b] Sandeep Kumar, [ID] [c] Anup Pandith, [ID] [d] M. N. Satyanarayan, [e] D. S. Shankar Rao, [ID] [f] S. Krishna Prasad [f] and Airody Vasudeva Adhikari [ID] *[a]

Herein, we report the design and synthesis of a new series of flying bird-shaped liquid crystalline (LC) cyanopyridone derivatives with a D–A–D architecture, **CPO-1** to **CPO-4**. Their mesomorphic, photophysical, electrochemical, and electroluminescence characteristics have been investigated in detail. Here, the H-bonding interactions through a central lactam core were shown to be the key driving force for their self-assembly into columnar mesophases. The key role of H-bonding has been confirmed by using newly synthesized similar shaped compounds, **MCP-1** to **MCP-3**. New **CPO** mesogens were found to be intense greenish blue light emitters with narrow band-gap energies. Conclusions were drawn based on theoretical studies also. Finally, the application potential of the selected mesogen **CPO-2** as an emissive material has been demonstrated for the fabrication of doped and non-doped OLED devices with different device architectures, which displayed encouraging results. In fact, this is the first report on the use of emissive H-bond-assisted columnar liquid crystals in devices. The present results provide a new guideline and a versatile approach to the design of new LC molecules for the fabrication of efficient OLEDs.

Introduction

The nano-segregation of disc-like molecules into one-dimensional columnar (Col) stacks through non-covalent interactions offers novel soft materials and they can be used as platform materials in the fabrication of various optical and electronic devices like photocopiers, photovoltaic cells, light-emitting diodes, laser printers, field-effect transistors and holographic data storage devices.[1–4] Recently, luminescent discotic liquid crystals (DLCs) have attracted increasing interest because of their unique self-organization behavior together with a combination of exceptional optophysical and anisotropic fluidic properties. However, to the

best of our knowledge, there are only a few reports available on the application of luminescent columnar liquid crystals in the field of OLEDs.[5–9] Currently, enormous effort has been made to realize emissive columnar mesogens, using the strategy of functionalizing the core with the necessary flexible periphery. Yet, there are still some challenges for constructing such new discotic mesogens with favorable electronic and optical properties.

Structurally, a variety of molecular architectures have been known to display columnar mesophases by dint of driving forces like π–π interactions, ionic interactions, van der Waals interactions, hydrogen bonding and charge transfer. In fact, columnar mesophases directed by H-bonding interactions are of particular importance, because their properties typically depend on the dynamics of H-bonding[10,11] and their high response towards external stimuli.[12–15] In such systems, the mesomorphic properties can be tuned by simple tailoring of the molecular structures. There are two possible ways for the construction of supramolecular LCs through H-bonding inter-actions, one is the step-wise assembly of disc-like entities which would organize into columns[16–21] whereas in the other case, molecules possessing polar and lipophilic units simultaneously arrange to form a large H-bonding network and undergo 2D nanoscale segregation without any intermediate step.[11,22–25] Until now, a large number of H-bonding scaffolds with appropriate designs have been investigated to obtain columnar mesophases.

[a] Organic Materials Laboratory, Department of Chemistry, National Institute of Technology Karnataka, Surathkal, Mangalore-575 025, India. E-mail: avachem@gmail.com, avachem@nitk.ac.in

[b] Department of Chemistry, Indian Institute of Technology Guwahati, Guwahati-781 039, India

[c] SCM group, Raman Research Institute, C.V. Raman Avenue, Sadashivanagar, Bangalore-560 080, India

[d] Department of Chemistry, Chonbuk National University, Jeonju, 54398, Republic of Korea

[e] Department of Physics, National Institute of Technology Karnataka, Surathkal, Mangalore-575025, India

[f] Centre for Nano and Soft Matter Sciences, Jalahalli, Bangalore-560 013, India

† Electronic supplementary information (ESI) available. See DOI: 10.1039/c8tc01737a
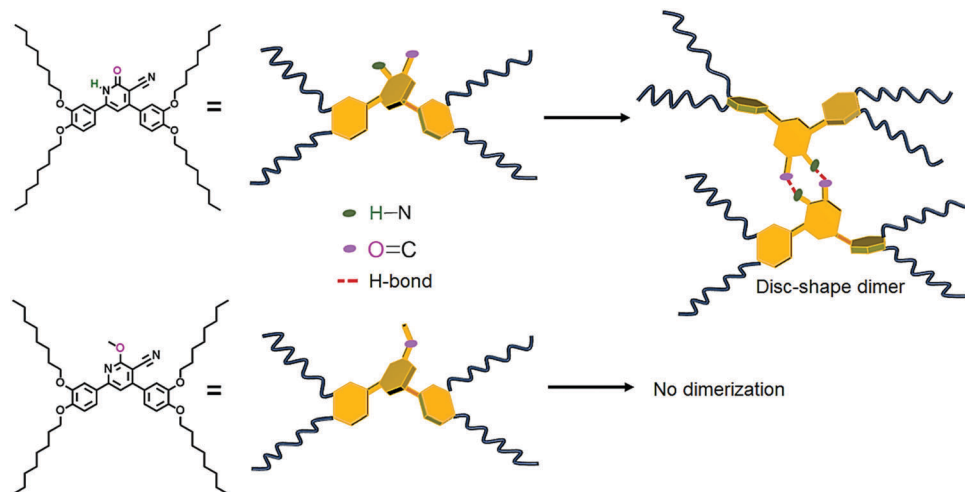
This journal is © The Royal Society of Chemistry 2018

J. Mater. Chem. C, 2018, **6**, 7385–7399 | 7385

Fig. 1 Schematic illustration of the formation of a disc-like structure dimer through desired H-bonding.

Among the various class of compounds, carboxylic acids, amides, pyridines, polyalcohols, carbohydrates, oligopeptides, pyrazoles, triazenes, melamines, *etc.* are widely studied H-bonding motifs.[4,25–27] Particularly, heteroaromatic systems capable of forming H-bonds are more advantageous as they deliver highly stable and ordered mesophases through well-defined H-bonding interactions.

Furthermore, the presence of donor–acceptor type structures provides good light absorption and/or emission characteristics for the mesogens, mainly due to push–pull induced intramolecular charge transport behavior. Moreover, in mesogens with the D–A architecture, the donor–acceptor interactions predominantly stabilize the self-assembly through extended conjugation. Consequently, these types of highly ordered self-assembled systems with preserved solid-state emission are considered to be potential candidates for organic light emitting diodes (OLEDs).[9,21]

In the literature, 2-pyridone derivatives have been studied extensively as bioactive materials,[28] intense luminogens[29,30] and dyes,[31,32] because of their favorable electronic properties and also, a few LCs based on 2-pyridone were reported.[16,33] Recently, we have investigated 3-cyano-2-pyridone (**CPO**) as a novel building block for the construction of highly luminous columnar mesogens, since the aforementioned heterocyclic core is a highly stable, fluorescent and powerful electron deficient system with synthetic versatility and the ability to form hydrogen bonds.

Motivated by the above-mentioned facts and in continuation of our research program on the development of novel luminescent pyridine-based liquid crystals,[34–37] we have designed a new series of D–A–D configured flying bird shaped mesogens (**CPO-1** to **CPO-4**) carrying electron deficient 3-cyano-2-pyridone as the central core substituted by two electron rich dialkoxy-phenyl rings at its 4th and 6th positions, keeping in mind that, the lactam core is expected to facilitate the formation of disc shaped H-bonded dimers. The newly designed molecules were successfully synthesized following simple and efficient synthetic protocols based on aromatic carbonyl compounds. All the new compounds were well-characterized by spectral and elemental analysis techniques. They showed columnar mesophases in a wide temperature range through dimerization by

means of hydrogen bonding between the two molecules *via* the central lactam core. In order to examine the role of H-bonding in the observed self-assembly, we synthesized similar shaped 2-methoxy-3-cyanopyridine derivatives (**MCP-1** to **MCP-3**) containing no CONH linkage in the ring but with the same substituents and studied them for their liquid crystalline properties; however, they fail to show any mesophase behaviour confirming the involvement of H-bonds in the self-assembly of flying bird-shaped **CPO-1** to **CPO-4** molecules, as shown in Fig. 1. The new mesogenic materials were investigated for their photophysical and electrochemical behavior. Accordingly, they were found to be deep bluish-green emitting materials with favorable HOMO and LUMO energy levels. Also, their theoretical study supports the observed low band gap. Based on these results, OLED devices have been fabricated using the new mesogens as emitters to study their electroluminescence performance. Finally, we have attempted to throw some light on the structure–property relationships of new mesogens with regard to their thermal, photophysical and electroluminescence behavior.

Results and discussion

Synthesis and characterization

The synthetic approach for the preparation of newly designed cyanopyridone based liquid crystals is depicted in Scheme 1. The intermediates, 3,4-dialkoxyacetophenones (**3a–d**), were prepared from catechol (**1**) by adopting Williamson's etherification method,[38] followed by Friedel Crafts acylation with acetyl chloride, in good yield. Other intermediates 3,4-dialkoxybenzaldehydes (**5a–d**) were synthesized from 3,4-dihydroxybenzaldehyde (**4**) by alkylation using the required *n*-alkyl bromides. Then, precursors **3a–d** were reacted with intermediates **5a–d** in the presence of ethyl cyanoacetate and in excess of ammonium acetate to yield symmetrically substituted compounds **CPO-1** to **CPO-4**, respectively. For synthesizing these cyanopyridones, precursors **3** and **5** substituted with similar alkoxy chains were used. Furthermore, 2-methoxy-3-cyanopyridine derivatives, **MCP-1** to **MCP-3,** were
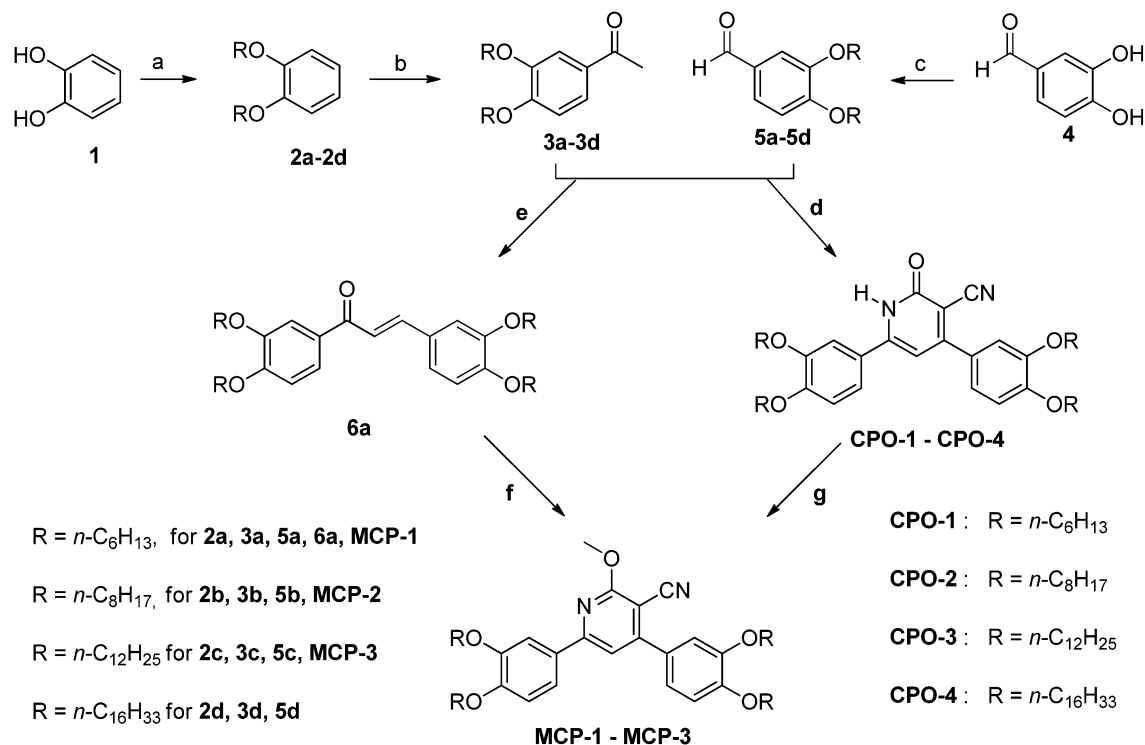
Scheme 1 (a) RBr, K_2CO_3, KI, DMF, 70 °C, 70–85%; (b) CH_3COCl, anhydrous $AlCl_3$, dry DCM, −5 to 0 °C, 85–92%; (c) K_2CO_3, RBr, DMF, 80 °C, 65–85%; (d) ethyl cyanoacetate, $AcONH_4$, EtOH, 70 °C, 25–40%; (e) aqueous KOH, EtOH, RT, 83%; (f) malononitrile, NaOMe, MeOH, RT, 40%; (g) MeI, K_2CO_3, DMF, 45 °C, 85–90%.

prepared separately using different synthetic protocols. Here, **MCP-1** was synthesized by Claisen–Schmidt condensation of aldehyde **3a** with ketone **5a** to give chalcone followed by cyclization of chalcone with malononitrile in the presence of sodium methoxide. Since its yield was poor, an alternate method was used to obtain **MCP-1**. In this method, compound **CPO-1** was directly alkylated with methyl iodide in the presence of a base to form **MCP-1** in good yield. The other two compounds **MCP-2** and **MCP-3** were synthesized in good yield by the latter method using a similar procedure. The chemical structures of the newly synthesized LC materials/intermediates were characterized by FTIR, ^{1}H-NMR, and ^{13}C-NMR spectroscopy and elemental analysis. The detailed synthesis procedures and characterization data are given in the ESI.†

Self-assembly and mesomorphic properties

The thermotropic phase behavior of the newly synthesized compounds **CPO-1** to **CPO-4** was investigated by using differential scanning calorimetry (DSC), polarised optical microscopy (POM) and temperature-variable X-ray diffraction (XRD) techniques. But compounds **MCP-1** to **MCP-3** were subjected to DSC analysis only. The phase transition temperatures and the associated enthalpy changes of **CPO-1** to **CPO-4** and **MCP-1** to **MCP-3** are summarised in Table 1.

Compound **CPO-1** bearing four *n*-hexyloxy peripheral tails melts at 89.48 °C (ΔH = 38.14 kJ mol^{-1}) to a mesophase, which clears at 153 °C with an energy change of 22.2 kJ mol^{-1} in the heating scan. It re-enters the mesophase at 148.51 °C

(ΔH = −15.51 kJ mol^{-1}) upon cooling, and this considerable higher enthalpy change may be attributed to the significant ordered packing of the molecules in the mesophase (Fig. 2c). It did not show any sign of crystallization until room temperature. Microscopic observations reveal that upon slow cooling from its isotropic phase, small birefringent batonnets started growing in the dark homeotropic region which further resulted in a wrinkle-free mosaic pattern. The same texture persisted until room temperature and it was not shearable as depicted in Fig. 2a and b. This is one of the characteristics revealed by the optical images of the columnar phases derived from classical discotics.

To get further insight into the structure of the mesomorphic morphology, temperature variable XRD studies have been carried out. The XRD patterns obtained for **CPO-1** throughout the mesophase range were almost similar. For instance, the spectrum obtained at 144 °C is shown in Fig. 2d. The spacings and the Miller indices of the peaks in these patterns are summarized in Table 2. In addition to the twelve sharp reflections over the low to middle angle region, a broad halo at 4.53 Å and a relatively sharp peak at 3.52 Å were seen in the wide angle region, the latter two being due to the fluidic nature of alkyl chains and aromatic core–core interactions, respectively. The indexing of the data to an oblique lattice provided the least differences between the experimental and calculated values, whereas attempts to fit a rectangular lattice resulted in substantial deviations. The obtained columnar phase with an oblique lattice has the lattice parameters, a = 26.85 Å and b = 23.34 Å with an

This journal is © The Royal Society of Chemistry 2018

J. Mater. Chem. C, 2018, **6**, 7385–7399 | 7387

Table 1 Phase transition temperatures and the corresponding enthalpies of **CPO-1** to **CPO-4** and **MCP-1** to **MCP-3**[a]

Compd.	Phase sequence	
	Heating	Cooling
CPO-1	Cr_1 89.48 (38.14) Col_{ob} 153.02 (22.2) I	I 148.51 (−15.51) Col_{ob}[b]
CPO-2	Cr_1 81.34 (9.28) Cr_2 88.74 (42.53) Col_{ho} 135.77 (4.06) Col_{hd} 149.14 (5.84) I	I 147.40 (−6.06) Col_{hd} 134.64 (−3.67) Col_{ho}[b]
CPO-3	Cr_1 91.10 (19.93) Cr_2 103.56 (74.95) Col_{ho} 120.36 (2.49) Col_{hd} 140.31 (6.31) I	I 138.96 (−6.02) Col_{hd} 122.12 (−1.86) Col_{ho}[b]
CPO-4	Cr_1 99.94 (38.27) Cr_2 107.90 (65.72) Cr_3 115.13 (43.43)	I 112.82 (−2.27) Col_{ho}[c] 50.33 (−18.39) Cr_4 40.84 (−14.19) Cr_5
MCP-1	Cr 81.55 (46.04) I	I 34.22 (−27.95) Cr
MCP-2	Cr 70.08 (58.16) I	I[b]
MCP-3	Cr 86.62 (82.19) I	I 31.27 (−58.62) Cr

[a] Peak temperatures/°C (enthalpies/kJ mol^{-1}) obtained by heating and cooling cycles at the rate of 5 °C min^{-1}. [b] Crystallization was not observed until room temperature. [c] The mesophase observed was monotropic; Cr_1, Cr_2, Cr_3, Cr_4 and Cr_5 are different crystalline solid phases; Col_{ho} = ordered columnar hexagonal phase; Col_{hd} = disordered columnar hexagonal phase and I = isotropic liquid phase.
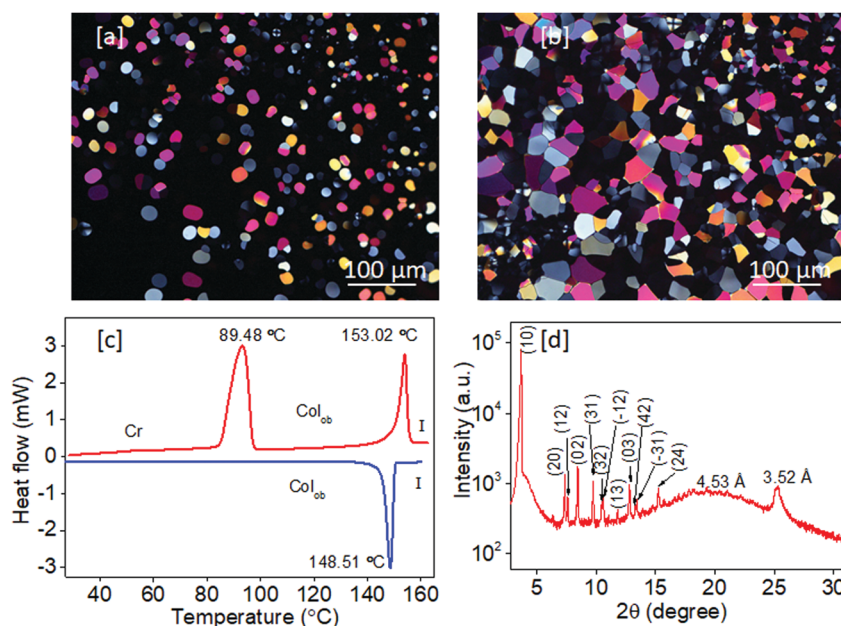

Fig. 2 POM images of **CPO-1**: (a) at 150 °C and (b) at 30 °C upon cooling from the isotropic phase; (c) DSC thermogram of **CPO-1** (red trace represents the heating cycle and blue trace represents the cooling cycle obtained at the rate of 5 °C min^{-1} under a nitrogen atmosphere); (d) XRD profile obtained for the Col_{ob} phase for compound **CPO-1** at 144 °C.

angle of 64.10°. Furthermore, the number of molecules per columnar slice (Z) was calculated as described in the literature.[39] For **CPO-1**, the value of Z was estimated to be 1.81, indicating that a pair of molecules constitutes a hexagonal lattice site. The lattice area S and molecular volume V were calculated to be 563.7 Å^2 and 1984.2 Å^3, respectively.

The second member of the series **CPO-2** showed two distinct crystalline transitions at 81.34 °C and 88.74 °C. A weak transition peak centred at 136 °C (ΔH = 4.06 kJ mol^{-1}) cleared at 149.14 °C (ΔH = 5.84 kJ mol^{-1}) to an isotropic liquid phase. In the cooling cycle, the two exothermic transitions at 147.4 °C (ΔH = −6.06 kJ mol^{-1}) and 134.64 °C (ΔH = −3.67 kJ mol^{-1}) were observed without any crystallization peak. This indicated the existence of two different mesophases as a function of temperature (Fig. 3a). Upon slow cooling from the isotropic phase, it developed a birefringent mosaic type texture at 141 °C. Upon further cooling at 120 °C, some of the birefringent texture became completely dark and these observations were consistent

with the DSC results (Fig. 3b and c). The observed textural changes suggest that there may be deviations in the packing order of the molecules in the mesophase.[40]

The XRD patterns obtained for both the LC phases of **CPO-2** were similar, but for the reflection due to core–core ordering. The diffraction pattern at 120 °C showed lower angle reflection peaks corresponding to Bragg's spacings of 26.08 Å, 15.62 Å, 13.08 Å, and 9.83 Å in the ratio of $1 : 1/\sqrt{3} : 1/2 : 1/\sqrt{7}$ and they can be indexed to the (10), (11), (20) and (21) planes of a hexagonal lattice. However in the wide angle region, the presence of a broad halo at 4.54 Å corresponds to the packing of flexible alkyl chains and the relatively sharp peak appeared at 3.50 Å is due to aromatic core–core interactions (Fig. 3d). The observed moderately smaller intracolumnar distance suggests that the LC phase is an ordered columnar hexagonal (Col_{ho}). However the reflection peaks (at 142 °C) obtained in a higher temperature mesophase range could be indexed to the same planes as assigned to the patterns obtained at 120 °C (Fig. 3d)

Table 2 XRD characterization data of **CPO-1** at 144 °C

Compd.	Phase (T/°C)	d_{obs} (Å)	d_{cal} (Å)	Miller indices (hk)	Lattice parameters a (Å), b (Å), lattice area S (Å^2), molecular volume V (Å^3)
CPO-1	Col$_{ob}$ (144)	24.15	24.15	(1 0)	a = 26.85
		12.04	12.08	(2 0)	b = 23.34
		11.66	11.67	(1 2)	γ = 64.10
		10.49	10.50	(0 2)	S = 563.7
		9.09	8.94	(3 1)	V = 1984.2
		8.46	8.40	(3 2)	Z = 1.81
		8.36	8.38	(−1 2)	
		7.50	7.68	(1 3)	
		6.92	7.00	(0 3)	
		6.66	6.63	(4 2)	
		6.59	6.61	(−3 1)	
		5.81	5.83	(2 4)	
		4.53(h$_a$)			
		3.52(h$_c$)			

d_{obs}, experimental lattice spacing; d_{cal}, calculated from the lattice parameters; a and b, lattice parameters deduced for Col$_{ob}$ with columnar tilt angle γ; h$_a$, alkyl chain correlation peak value; h$_c$, core–core spacing; Z, number of molecules per columnar slice; S, lattice area; and V, molecular volume.

for Col$_{hd}$. However, the core–core correlation peak is very weak and it occurs at a higher spacing value of 3.64 Å. Therefore, this LC phase was assigned as the disordered columnar hexagonal, Col$_{hd}$ (Fig. 3e). The hexagonal cell parameter a was found to be 30.11 Å and 29.20 Å for Col$_{ho}$ and Col$_{hd}$, respectively. On the basis of the XRD data obtained at 120 °C assigned to Col$_{ho}$, the columnar cross-section area S and the molecular volume V were found to be 7854 Å^2 and 2670.3 Å^3, respectively. The value of Z for these two columnar hexagonal phases[41] was found to be 2.0. The detailed XRD characterization data are given in Table 3.

Wide-angle XRD patterns of **CPO-2** were acquired at different temperatures upon heating as well as upon cooling respectively (Fig. S27, in ESI†). As the temperature increases, the aromatic stacking reflection becomes gradually weaker, an abrupt broadening at 140 °C (endset of the transition peak for Col$_{ho}$ to Col$_{hd}$) takes place and it continues till the isotropic phase, which indicates the intracolumnar transition from ordered to the disordered packing of the discs. Furthermore, we plotted temperature-dependent layer spacing against the intensity of the (10) peak (Fig. 3f). From the graph, it is evident that both parameters exhibit clear changes at the transition between the two columnar phases. The dashed lines indicate the transition temperature as obtained from DSC scans. The layer thickness calculated from the (10) peak shows a significant increase right from the isotropic phase, which presents an "inflection point" variation in the vicinity of this intracolumnar transition, and at
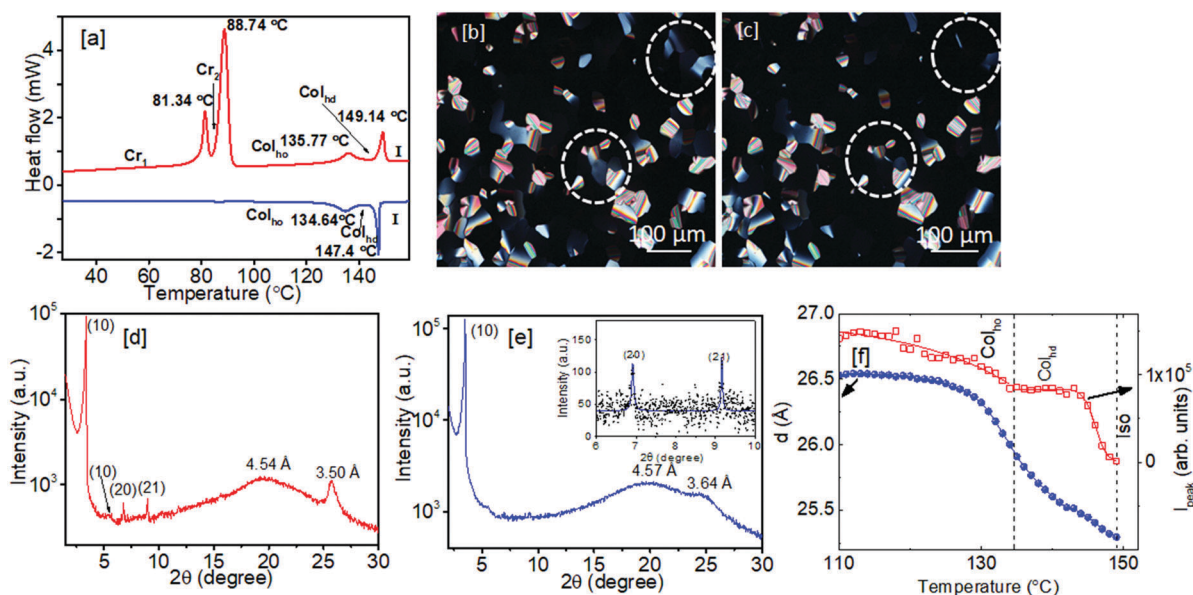

Fig. 3 (a) DSC thermogram of **CPO-2** (red trace represents the heating cycle and blue trace represents the cooling cycle obtained at 5 °C min^{-1} under a nitrogen atmosphere); POM images of **CPO-2** at (b) 141 °C and (c) 120 °C captured upon cooling from the I phase (the circular region indicates the change of texture); XRD profiles obtained for **CPO-2** at (d) 120 °C and (e) 142 °C; (f) plot of temperature vs. layer spacing and the peak intensity of the (10) peak.

This journal is © The Royal Society of Chemistry 2018

J. Mater. Chem. C, 2018, **6**, 7385–7399 | 7389

Table 3 XRD characterization data of **CPO-2** to **CPO-4** at different temperatures

Compounds	Phase (T/°C)	d_{obs} (Å)	d_{cal} (Å)	Miller indices (hk)	Lattice parameter a (Å), lattice area S (Å^2), molecular volume V (Å^3)
CPO-2	Col$_{ho}$ (120)	26.08	26.08	(10)	a = 30.11
		15.62	15.05	(11)	S = 785.4
		13.08	13.03	(20)	V = 2670.3
		9.83	9.85	(21)	Z = 2.0
		4.54 (h$_a$)			
		3.50 (h$_c$)			
	Col$_{hd}$ (142)	25.29	25.29	(10)	a = 29.20
		12.61	12.64	(20)	S = 738.5
		9.55	9.55	(21)	V = 2658.7
		4.57 (h$_a$)			Z = 2.0
		3.64 (h$_c$)			
CPO-3	Col$_{ho}$ (110)	28.25	28.25	(10)	a = 32.62
		16.30	16.05	(11)	S = 921.5
		14.07	13.76	(20)	V = 3179.2
		10.67	10.47	(21)	Z = 1.9
		4.52 (h$_a$)			
		3.45 (h$_c$)			
	Col$_{hd}$ (130)	27.84	27.84	(10)	a = 32.14
		16.05	16.07	(11)	S = 894.9
		13.76	13.91	(20)	V = 3150.3
		10.47	10.52	(21)	Z = 1.9
		4.53 (h$_a$)			
		3.52 (h$_c$)			
CPO-4	Col$_h$ (108)	33.34	33.34	(10)	a = 38.49
		19.12	19.24	(11)	S = 1283.5
		16.57	16.66	(20)	V = 4453.8
		12.68	12.60	(21)	Z = 2.1
		4.52 (h$_a$)			
		3.47 (h$_c$)			

d_{obs}, experimental lattice spacing; d_{cal}, calculated from the lattice parameter, a for the hexagonal lattice; h_a, alkyl chain correlation peak value; h_c, core–core spacing; Z, number of molecules per columnar slice; S, lattice area; and V, molecular volume.

much lower temperatures it exhibits a limiting behavior. Interestingly, the peak intensity of the (10) reflection also exhibits clear changes marking the Col$_{ho}$–Col$_{hd}$ transition.

The compound **CPO-3** bearing fourfold dodecyl chains melts completely at 103.56 °C (ΔH = 74.95 kJ mol^{-1}) followed by the weak endothermic transition at 120.36 °C (ΔH = 2.49 kJ mol^{-1}) and then clears at 140.31 °C (ΔH = 6.31 kJ mol^{-1}). It was not crystallized upon cooling until room temperature (Fig. 4a). The textural observations on slow cooling indicated the existence of columnar mesomorphism (Fig. 4b and c). The XRD patterns obtained at different temperatures over the entire mesophase range confirmed that the weak transition within the mesophase range is an intracolumnar transition of a columnar hexagonal mesophase.

The XRD trace of **CPO-3** at 110 °C is depicted in Fig. 4d and the observed small angle reflection peaks are assigned to the columnar hexagonal lattice. However, a broad diffused maximum at a spacing of 4.53 Å is attributed to the conformational disorder of the peripheral chains and a moderately sharp peak at 3.45 Å is due to the ordered stacking of aromatic segments. At 130 °C, **CPO-3** showed similar reflection patterns except for the peak due to intracolumnar spacings, which was observed at 3.52 Å (Fig. 4e). Therefore, the higher temperature mesophase can be assigned to Col$_{hd}$ and the lower temperature mesophase to Col$_{ho}$. Furthermore, wide-angle XRD spectra were recorded at different temperatures in

Col$_{ho}$ and Col$_{hd}$ mesophase ranges (Fig. S28, in ESI†). Evidently, the core–core peak intensity and its position throughout the two thermal mesophase ranges, as well as its changes at the transition temperatures further confirm the intracolumnar transitions. The conformational motions of mesogenic units within the columnar axis can be further confirmed by examining the FWHM of the peak which signifies the intracolumnar distance. The plot of full width at half maxima (FWHM) of the core–core peak as a function of temperature for one of the compounds, **CPO-3,** is shown in Fig. 4e. In the Col$_{ho}$ phase range, the FWHM show negligible changes, whereas an abrupt increase at 125 °C and continuation of the same trend at a higher temperature confirm intercolumnar changes. The results are fairly consistent with the DSC transitions.

The DSC thermogram of **CPO-4** carrying longer n-hexadecyloxy substitutions demonstrates the monotropic mesophase behavior as shown in Fig. 5a. In the cooling cycle, I-LC transition was observed, which was confirmed by the growth of birefringent mosaic type small domains upon cooling from its isotropic phase (Fig. 5c). Indeed, the X-ray pattern contains a set of four maxima in the low-angle region (Table 3) with the reciprocal ratio of $1 : 1/\sqrt{3} : 1/2 : 1/\sqrt{7}$ which can be indexed to the (10), (11), (20) and (21) planes of a hexagonal lattice with lattice parameter a = 38.49 Å.

The thermotropic phase behavior of **CPO-1** to **CPO-4** reveals that an increase in peripheral chain lengths has led to the

7390 | J. Mater. Chem. C, 2018, **6**, 7385–7399

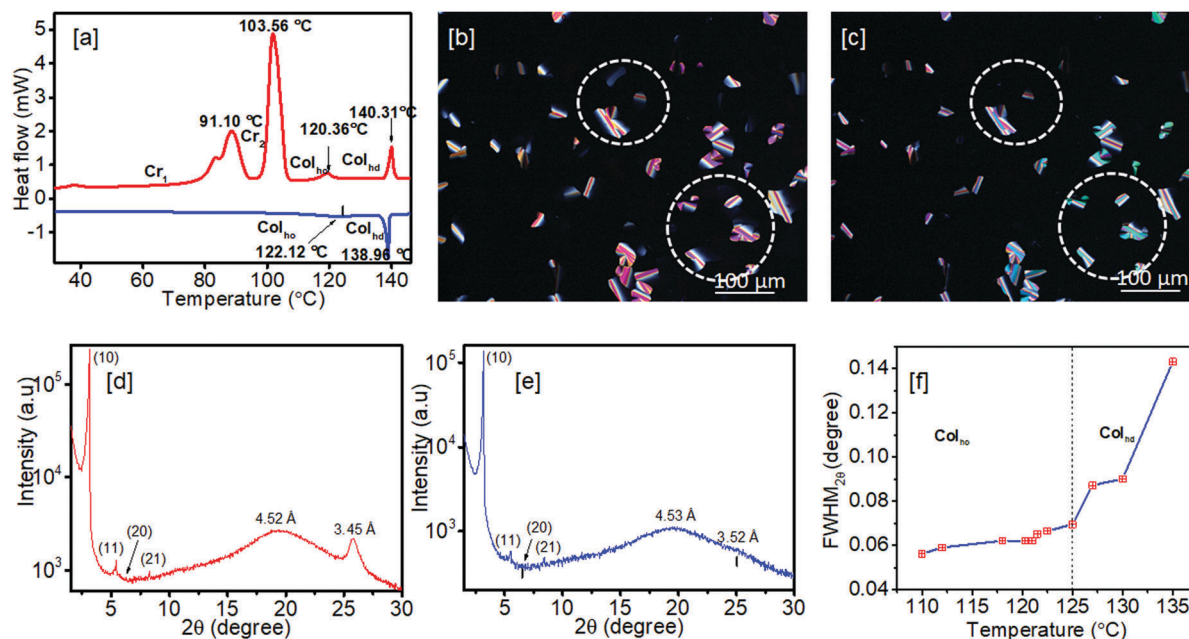This journal is © The Royal Society of Chemistry 2018

Fig. 4 (a) DSC thermogram of **CPO-3** (red trace represents the heating cycle and blue trace represents the cooling cycle obtained at 5 °C min^{-1} under a nitrogen atmosphere); POM images of **CPO-3** captured upon slow cooling from the I state at (b) 135 °C and (c) 100 °C; XRD profiles obtained for the compound **CPO-3** at (d) 110 °C and (e) 130 °C; (f) variation of the FWHM of the aromatic stacking peak as a function of temperature.
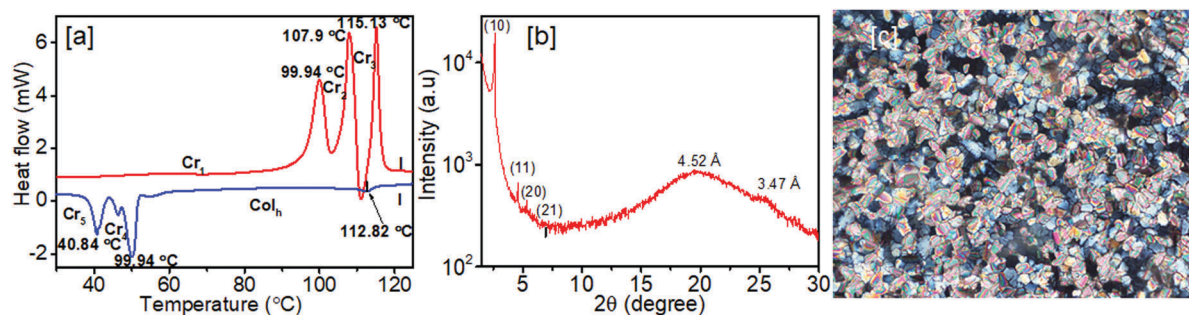

Fig. 5 (a) DSC thermogram of **CPO-4** (red trace indicates the heating cycle and blue trace indicates the cooling cycle obtained at 5 °C min^{-1} under a nitrogen atmosphere); (b) XRD profile obtained for **CPO-4** at 100 °C; (c) optical texture observed for Col$_h$.

destabilization of their mesomorphic nature. Interestingly, **CPO-1** with four hexyloxy chains displayed a columnar oblique exclusively. However in **CPO-2**, increasing the chain length by two methylene groups demonstrates two distinct columnar hexagonal mesophases, which may be probably due to an increase in the diameter size of the overall disc. Depending on the molecular order along the columnar axis, **CPO-2** and **CPO-3** (dodecyloxy substituted) exhibited an intracolumnar transition from Col$_{ho}$ to Col$_{hd}$ phases. Thus, the chain length plays a key role in deciding the symmetry of Col phases observed in these types of mesomolecules. The enthalpy changes observed for an order to disordered columnar transitions of **CPO-2** and **CPO-3** were noted to be 4.06 kJ mol^{-1} and 2.49 kJ mol^{-1}, respectively. The observed high enthalpy values for the weaker columnar transitions are attributed to strong intermolecular H-bonding as well as dipolar interactions owned by the mesogens in the Col$_{ho}$ phase. Then, it requires a substantial energy to disturb the molecular ordering. Hence,

such intracolumnar changes can be assigned to be first order transitions,[40] but similar changes were also reported to be second order transitions.[42] Besides, the data indicate the system's tendency to have a Col$_{ho}$ phase, as the chain length is increased. This could be owing to well establishment between the strongly correlated H-bonded core region and the floppy hydrocarbon regions.

According to the XRD results, columnar mesophases generated by **CPO-1** to **CPO-4** consist of two molecules per slice of column ($Z = 2$). So, we assumed that the central cyanopyridone ring might have involved in the formation of dimers through intermolecular H-bonding to yield disc-shaped structures. In order to validate this assumption, we synthesized one more series of molecules, **MCP-1** to **MCP-3**, by replacing the central cyanopyridone unit with 2-methoxy-3-cyanopyridine, which are devoid of H-bonding sites (Scheme 1). However, they do not display any mesomorphism, as confirmed by DSC traces (Fig. S29, in the ESI†), which clearly indicates the role of the central core in dimer formation. Conclusively, the H-bonding
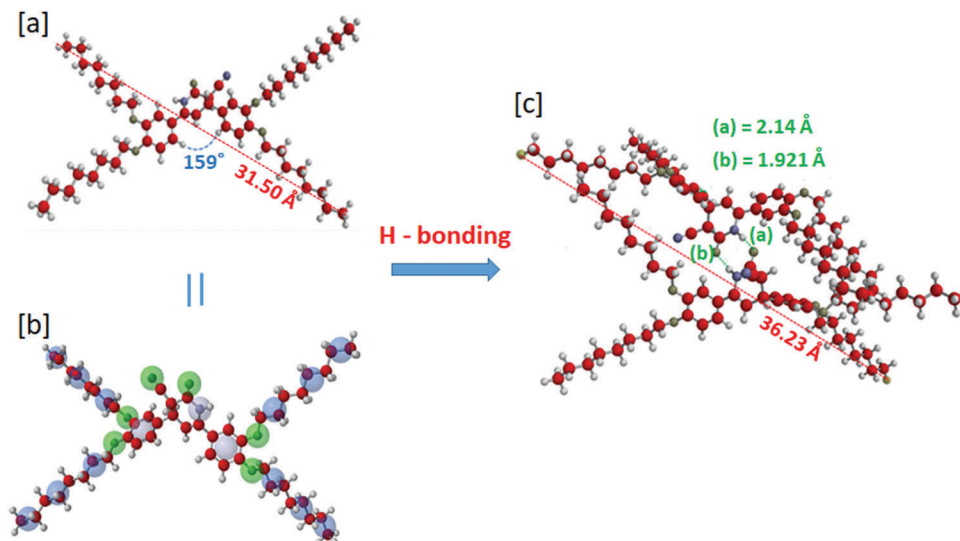
Fig. 6 (a) DFT based energy-minimized structure of **CPO-2**; (b) energy-minimized structure of **CPO-2** showing chemical functional descriptors (CFDs); (c) energy-minimized structure of the H-bonded dimer for **CPO-2**.

interaction is the deciding factor for the formation of mesophases in the bird-shaped cyanopyridones.

Molecular modeling

Molecular models have been proposed for the columnar meso-phases of new cyanopyridones using XRD data and density functional theory (DFT) calculations. The DFT calculations were performed at the B3LYP/6-31G* level of theory using the Spartan 10 software in a vacuum. According to theoretical simulations of the **CPO-2** molecule, the conjugatively connected two dialkoxyphenyl rings are not co-planar with the central cyanopyridone ring, wherein lactam and dialkoxyphenyl rings are at the top and lower sides, respectively, with a dihedral angle of 159°. The observed average end to end diagonal distance was found to be 31.50 Å. An overall geometry seems to be a flying bird shape.

As discussed in the preceding section, H-bonding plays a key role among the non-covalent interactions in the molecular self-assembly of the **CPO** molecules. Such an important interaction can be theoretically studied by the chemical functional description method (CFD); thereby it is possible to observe the potential electron acceptor/donor and proton donor/acceptor sites in the molecules. Fig. 6a depicts the DFT based energy-minimized structure of the **CPO-2** molecule and Fig. 6b portrays chemical functional descriptors (CFDs), wherein the various blue regions represent the proton donor sites that include the NH group of the lactam ring and alkyl carbon atoms, while the green regions signify the proton acceptor sites located on carbonyl oxygen, CN and ether linkages. Therefore, this efficient proton donor and acceptor nature facilitates the formation of strong H-bonding to form a cyclic structure between two cyanopyridone rings. To understand the structural conformations of **CPO**-based dimeric segments in the columnar mesophase, an energy-minimized structure of an H-bonded dimeric unit for **CPO-2** has been obtained. As visualized in Fig. 6c, one of the dioctyloxyphenyl rings from each of the **CPO-2** units rotates with respect to the

cyanopyridone ring at ∼90° when compared to its monomeric counterpart for stabilizing the dimeric structure. According to simulations, the obtained intermolecular hydrogen bonding distances between the oxygen atom of the C=O group and the amidic proton CO–NH of the adjacent lactam ring (labelled a and b in green colour) are 2.104 Å and 1.921 Å, respectively. The maximum end to end diagonal distance was found to be 36.234 Å.

As XRD results and theoretical simulations of **CPO-1** reveal that the two molecules undergo space filling dimerization, which further stack into columns with an intermolecular spacing of 3.52 Å. The resulting columns are arranged in an oblique lattice. Since the angle of the lattice sides is 64.11° ≠ 90°, the shape of the lattice would be a parallelogram as demonstrated in Fig. 7.

As mentioned in the previous section, the mesogens **CPO-2** and **CPO-3** display two distinct columnar hexagonal meso-phases as a function of temperature. The hexagonal cell para-meter 'a' for Col_{ho} and Col_{hd} phases of **CPO-2** was found to be 30.11 Å and 29.20 Å, respectively and these values are 17% and 20% smaller than the average diameter of the H-bonded dimeric unit. This may be due to intercalation and/or folding of the alkyl chains. Moreover, these observations are mainly due to the changes in their intracolumnar spacings. Such transitions in these propeller-like mesogens are known to be ascribed to conformational motions, which increase the meso-genic fluctuations along the columnar axis, resulting in the changes in intercolumnar ordering. Keeping these things in mind, it can be considered that, in the Col_{hd} phase the discs are within a column whose positions are truly liquid-like, but gain significant correlation in the Col_{ho} phase. The liquid-like correlations in the former appear to permit tilting of the discs within the column, a feature that could also be responsible for a much lower intercolumnar distance, when compared to the model-determined length of the dimer. Understandably, the ordering of the discs in the Col_{ho} phase reduces this degree of
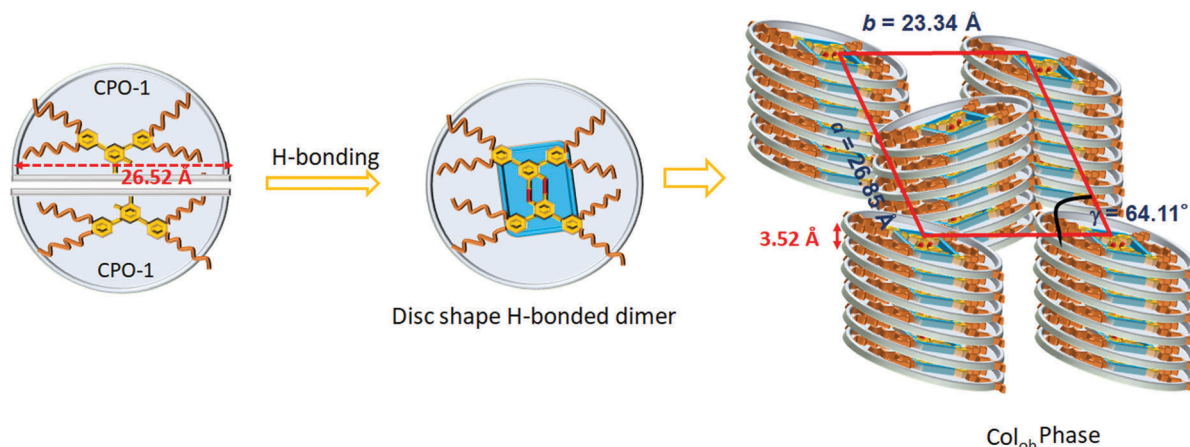
Fig. 7 Schematic representation of the self-assembly of **CPO-1** in the Col_{ob} phase (for the XRD patterns obtained at 144 °C).

freedom causing the spacing to increase by ~1.0 Å. Fig. 8 schematically illustrates the self-assembly of **CPO-2** molecules in an ordered and disordered columnar hexagonal mesophase.

Variable-temperature FTIR studies

The formation of disc-like dimeric structures in these cyanopyridone derivatives through intermolecular H-bonding was further confirmed experimentally using variable-temperature FTIR analysis. Representatively, the spectra for **CPO-1** and **CPO-2** were obtained with KBr pellets at different temperatures, upon slow cooling from their isotropic phase to the crystalline state through the mesophase range, according to DSC results. Since the non-relaxed N–H stretching band of the central lactam ring

was not observed in all different states, the significant absorption band due to C=O stretching was considered in the present study.[43] In the isotropic state, **CPO-1** displayed a strong absorption band due to C=O stretching at 1641 cm^{-1}. However, it showed an absorption band at around 1648 cm^{-1} at different temperatures throughout the mesophase range (Fig. 9(left)). Since the compound was not crystallized immediately, the absorption band appeared in the same region. In order to examine the nature of H-bonding in its crystalline state, the FTIR spectra for the same KBr pellet sample were recorded after 48 hours. In the spectra, the C=O$_{str}$ band was observed at 1658 cm^{-1}. It was noticed that there was a considerable shift in the C=O$_{str}$ band from the liquid crystalline phase to the crystalline state, which
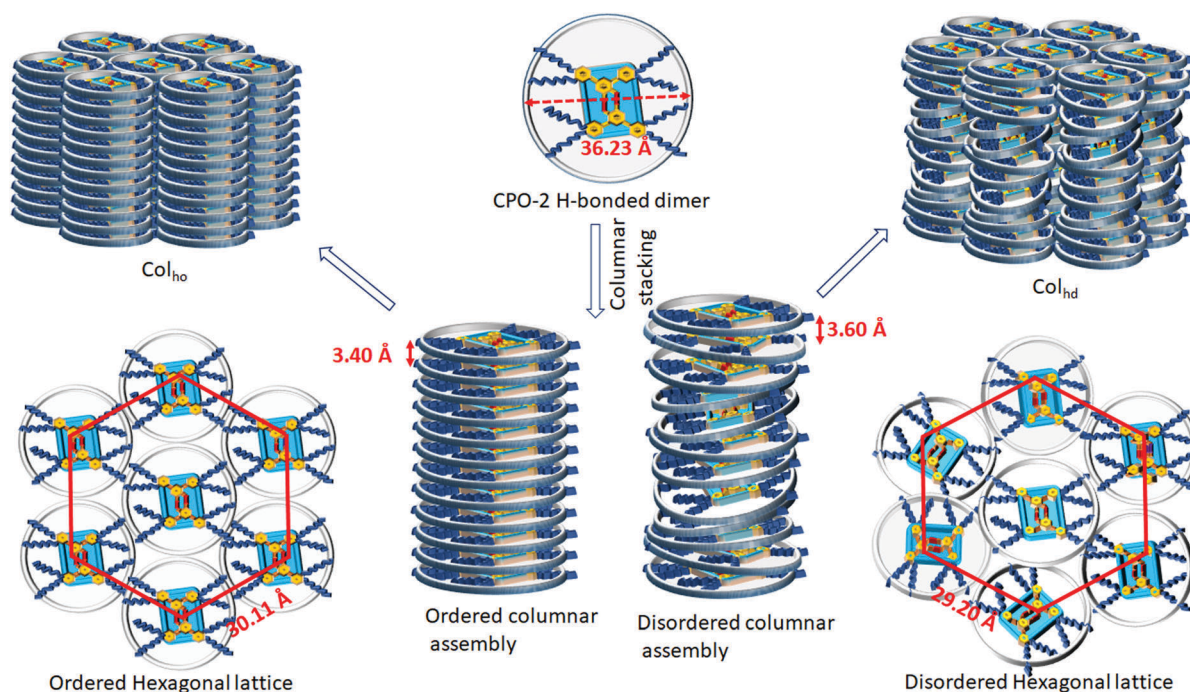

Fig. 8 Schematic demonstration of the self-assembly of **CPO-2** in an ordered and disordered columnar hexagonal mesophase (for the XRD patterns obtained at 120 °C and 142 °C).
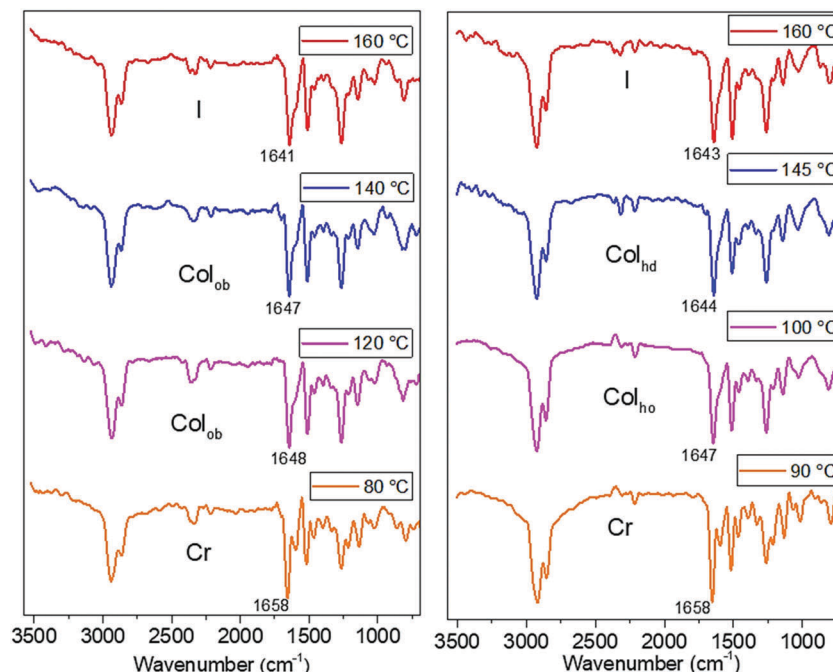
Fig. 9 FTIR spectra (KBr) in different phases of **CPO-1** (left spectra) and **CPO-2** (right spectra).

Table 4 Photophysical characterization data

Compd.	$\lambda_{abs}{}^a$ (nm)	$\lambda_{em}{}^a$ (nm)	Stokes shift^a (cm^{-1})	$E_{g\ opt}{}^b$ (eV)	$\Phi_F{}^{a,c}$	$\lambda_{em}{}^d$ (nm)	τ^e (ns) $\tau_1/\tau_2/\tau_3$
CPO-1	234, 261, 383	454	4083	2.82	0.21	486	0.11/0.85/2.56
CPO-2	234, 261, 383	454	4083	2.83	0.22	482	0.11/0.88/2.85
CPO-3	233, 261, 382	453	4103	2.85	0.21	480	0.12/0.89/2.91
CPO-4	235, 260, 381	453	4171	2.87	0.19	478	0.13/0.92/3.12

^{a} Determined for solution in dichloromethane (2×10^{-5} M). ^{b} Optical band gap estimated by the red edge of the absorption band in the UV-visible spectrum. ^{c} Relative quantum yield determined with respect to quinine sulphate solution in 0.1 M H_2SO_4 with a quantum yield of 0.54. ^{d} Emission maxima of the spin-coated thin film. ^{e} Fluorescence life time with λ_{exc} = 350 nm.

unambiguously confirmed the presence of intermolecular H-bonding in the mesophase. Consequently, **CPO-1** undergoes dimerization through inter molecular H-bonding to yield disc-shaped structures. Similar observations were made in the case of **CPO-2** also. In the FTIR spectra of **CPO-2**, C=O$_{str}$ bands were perceived at 1643, 1644, 1647 and 1658 cm^{-1}, in I-, Col$_{hd}$, Col$_{ho}$ and Cr phases, respectively (Fig. 9(right)). This observation has confirmed the presence of intermolecular H-bonding to form a dimer in its mesophase. Thus, the obtained FTIR results strongly support the model for the self-organization of **CPO-2** in the mesophase as discussed in the previous section.

Photophysical properties

The potentiality of the newly synthesized LC materials for optoelectronic applications has been investigated by their photophysical studies. Both UV-visible absorption and emission spectra were recorded for **CPO-1** to **CPO-4** solutions in DCM ($c = 2 \times 10^{-5}$ M) and the results are summarised in Table 4. Structurally, all the mesogenic materials differ only in the length of the alkyl chains, which has a minimum effect on their energy of absorption and emission. Consequently, all these D–A–D type materials exhibit analogous absorption and emission bands.

They display one absorption maximum (λ_{abs}) in the range of 381–383 nm, attributed to n–π^* transition and the two shoulder bands (231–236 and 267–267 nm) due to π–π^* transition (Fig. 10a). Their emission spectra were recorded upon excitation at their respective absorption maxima (λ_{abs}).

All members of the series displayed emission maximum (λ_{em}) at around 454 nm as shown in Fig. 10b, with a Stokes shift of about 71 nm. The optical band gaps ($E_{g,op}$) were calculated by using the equation, $E_{g,op} = 1242/\lambda_{onset,abs}$ eV, where $\lambda_{onset,abs}$ is the onset wavelength of their respective absorption spectrum and is found to be in the range of 2.82–2.87 eV. The same solution samples in quartz containers were kept under illumination of 365 nm light in a UV chamber and the emission was photographed. A deep bluish green emission was observed and their corresponding photos are shown in Fig. 10d. The fluorescence lifetimes of **CPO-1** to **CPO-4** at 2×10^{-5} M concentration in DCM were measured using a time-correlated single photon counting technique and the observed decay profiles are shown in Fig. 10c. The fluorescence lifetimes (τ) of the excited species formed were measured by monitoring their emission maxima. The decays fitted tri-exponentially with three excited species for all the solution samples in the range
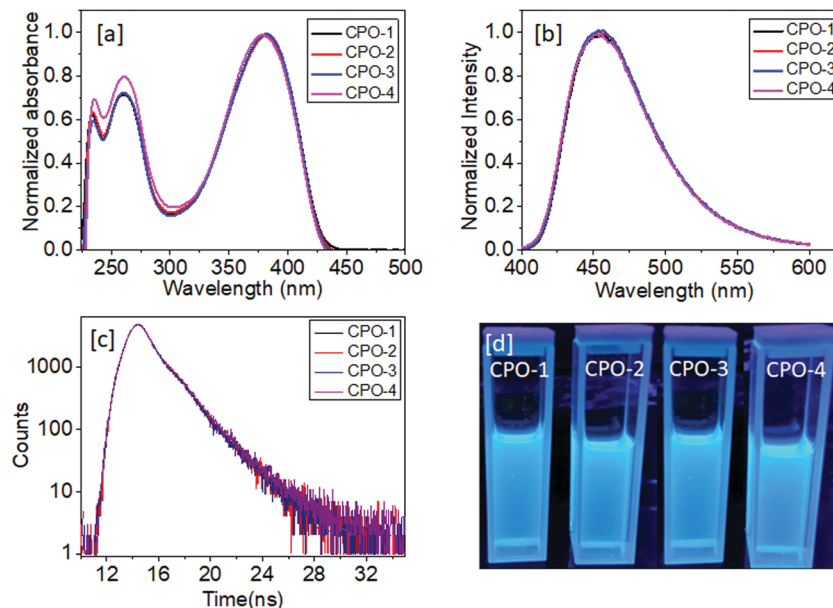
7394 | J. Mater. Chem. C, 2018, **6**, 7385–7399

This journal is © The Royal Society of Chemistry 2018

Fig. 10 (a) UV-visible absorption spectra of samples; (b) fluorescence spectra (excited at their respective λ_{abs}); (c) time-resolved fluorescence decay profile and (d) the emission hue for sample solutions under 365 nm irradiation.

of 0.1–0.13, 0.85–0.92 and 2.56–3.12 ns, respectively. The fluorescence quantum efficiency values of these materials were estimated by a relative method. Their quantum yields were calculated with respect to quinine sulfate solution (0.1 M H2SO4).[44–46] The quantum efficiency of the compounds was found to be in the range of 0.19–0.22.

In order to examine the photophysical properties of the new LC materials in solvents with different polarity, we examined the absorption and emission behavior of a representative compound, **CPO-1**, in various solvents with different polarities. The resulting spectra and their corresponding data are given in the ESI† (Fig. S30). The dilute solutions of **CPO-1** have not shown any significant changes with respect to solvent polarity

in their absorption as well as emission behaviors. The results reveal that both its ground and excited states are nearly non-polar in nature.

Furthermore, in order to study the photophysical properties of new LC materials in the solid state, good-quality thin films of the samples were obtained on quartz plates from their DCM solutions, following a spin coating technique. Their emission spectra were obtained upon excitation at their λ_{abs}, obtained from their corresponding solution states (Fig. 11a). The samples displayed the emission band maxima in the range of 478–486 nm, with a bathochromic shift of ∼25 nm when compared to their respective maxima in the solution state. This is attributed to their molecular aggregation in the film state. Upon irradiation with
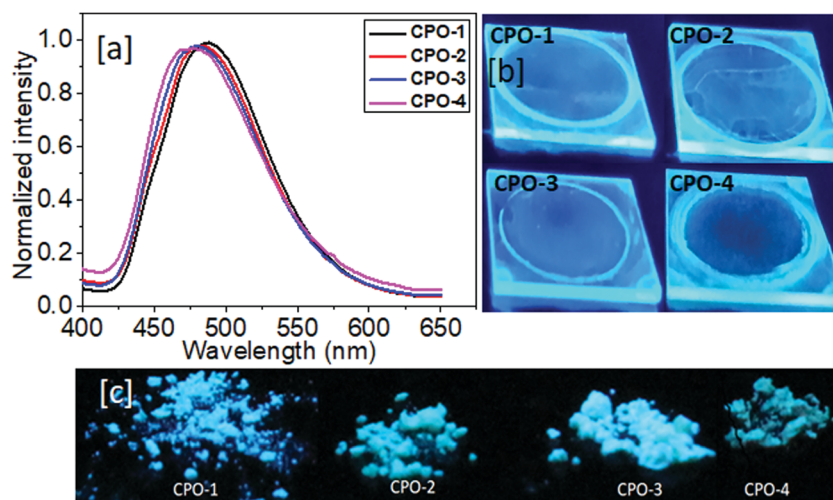

Fig. 11 (a) Fluorescence spectra of spin-coated thin films of samples; (b) the emission hue of the same thin films under 365 nm UV irradiation and (c) powder samples.

Table 5 Electrochemical data[a]

Compd.	$E_{1\text{red}}{}^{b}$ (V)	$E_{1\text{oxd}}{}^{c}$ (V)	$E_{\text{LUMO}}{}^{d}$ (eV)	$E_{\text{HOMO}}{}^{e}$ (eV)	$E_{\text{g,CV}}{}^{f}$ (eV)
CPO-1	−0.68	1.32	−3.62	−5.62	2.00
CPO-2	−0.66	1.29	−3.64	−5.59	1.95
CPO-3	−0.64	1.31	−3.66	−5.61	1.95
CPO-4	−0.65	1.33	−3.65	−0.5.63	1.98

[a] Recorded in 1×10^{-3} M DCM solution. Experimental conditions: glassy carbon as a working electrode, Ag/AgCl as a reference electrode, platinum wire as a counter electrode, TBAP (0.1 M) as a supporting electrolyte, and scanning rate: 50 mV s^{-1}. [b] Onset potential of reduction. [c] Onset potential of oxidation. [d] Estimated by using the formula $E_{\text{LUMO}} = -[4.8 - E_{1/2,\text{Fc/Fc}^+} + E_{1\text{red}}]$ eV. [e] Estimated by using the formula $E_{\text{HOMO}} = -[4.8 - E_{1/2,\text{Fc/Fc}^+} + E_{1\text{oxd}}]$ eV, where $E_{1/2,\text{Fc/Fc}^+}$ was found to be 0.50 V. [f] Calculated from the formula $E_{\text{g,CV}} = E_{\text{LUMO}} - E_{\text{HOMO}}$.

365 nm UV light, these LC materials in bulk, as well as thin films, emit visually perceivable bright bluish green color, as seen in Fig. 11b and c.

Electrochemical properties

The energy levels of frontier orbitals (HOMO and LUMO) of these new LC materials were estimated by the cyclic voltammetry (CV) method. The CV measurements were carried out by using 1 mM solution of **CPO-1** to **CPO-4** in dry DCM containing tetrabutyl-ammonium perchlorate (0.1 M) as the supporting electrolyte. The experimental conditions and the obtained electrochemical data are tabulated in Table 5. All the compounds displayed irreversible oxidation and reduction curves (Fig. S31, ESI†). The energy levels of HOMO and LUMO orbitals were calculated by using the formula $E_{\text{HOMO}} = -[4.8 - E_{1/2,\text{Fc/Fc}^+} + E_{1\text{oxd}}]$ eV and $E_{\text{LUMO}} = -[4.8 - E_{1/2,\text{Fc/Fc}^+} + E_{1\text{red}}]$ eV. The energy levels of the HOMO and the LUMO of the materials were estimated to be in the range of −5.59 to −5.63 and −3.62 to −3.66 eV, respectively, with the band gap range of 1.95–2.0 eV. From the data, it is clear that the calculated electrochemical band gap values were found to be smaller than the optical band gaps of all the materials.

Fig. 12 (a) HOMO, LUMO and band gap energies; (b) MEPs showing the ground state dipole moments and charge distributions (Red→Blue indicates negative to positive potentials).

Theoretical HOMO–LUMO analysis

In order to realize the frontier molecular orbital (FMO) distributions and their theoretical energy in the newly synthesized **CPO** molecules, we carried out the DFT studies at the B3LYP/6-31G* level of theory using the Spartan 10 software. We have chosen one of the molecules *i.e.* **CPO-2** for theoretical simulation. As discussed earlier, the full geometry optimized structure of **CPO-2** is similar to a flying bird kind of shape (Fig. 6a). According to theoretical simulations, the HOMOs localized throughout the aromatic domain, whereas the LUMOs distributed only on the cyanopyridone ring (Fig. 12a). This significant intramolecular charge transfer (ICT) has led to efficient light emission in the blue region. The calculated band gap energies were corroborated with the electronic transitions observed in the UV-visible spectra. However, the energy of HOMO and LUMO levels showed a variation of about 1.5 eV when compared to their experimentally determined values. This could be due to the solvent as well as counter ion effects in the electroanalytical technique. Because of the technical limitations in the DFT based energy minimized structure calculations, it was not successful in the solvent model. Such deviations could be attributed to solvents, pH, temperature, and ionic strength as well as the solid surface of electrodes during the electron transfer process. The obtained HOMO and LUMO distributions and the molecular electrostatic potential map (MEP) validated the clear electronic distributions with a relatively high ground state dipole moment (5.53 Debye) oriented towards the electron deficient cyanopyridone unit (Fig. 12b).

Electroluminescence properties

The electroluminescence performance of the selected LC material, *i.e.* **CPO-2** with the highest quantum efficiency, was evaluated in the fabricated OLED devices, as an emitting material. In the present study, four different device architectures, *viz.* devices A, B, C and D with configurations ITO/PEDOT: PSS/**CPO-2**/LiF/Al, ITO/PEDOT: PSS/PVK: **CPO-2**/LiF/Al, ITO/PEDOT: PSS/PVK: **CPO-2**/BCP/Alq$_3$/LiF/Al and ITO/PEDOT: PSS/PVK/PVK: **CPO-2**/BCP/Alq$_3$/LiF/Al, respectively, were fabricated.

In the case of device A, **CPO-2** acted as a sole emitter, whereas for devices B, C, and D, 10 wt% of **CPO-2** was doped in PVK (poly(9-vinylcarbazole)) acted as an emitter. Here, PVK was used because of its good miscibility with numerous emitting materials and excellent film-forming capability.[9] The energy level diagram of the OLEDs and the different device configurations used in this study are shown in Fig. 13. In the devices, patterned indium tin oxide (ITO) coated glass substrate acts as a transparent anode. Poly(3,4-ethylenedioxy-thiophene)/poly(styrene-sulfonate) (PEDOT:PSS) was used as a hole injection material. It has the ability to smoothen the ITO surface which in turn decreases the turn-on voltage and reduces the probability of electrical shorts and hence extends the lifetime of the device. The performance data of new OLEDs are tabulated in Table 6. The current density–voltage–luminance (J–V–L) characteristics are shown in Fig. 14a.

The device A composed of **CPO-2** as an emitter showed very weak emission. However, device B composed of **CPO-2** (10 wt.%) as a dopant in the PVK host as an emitting material shows a high
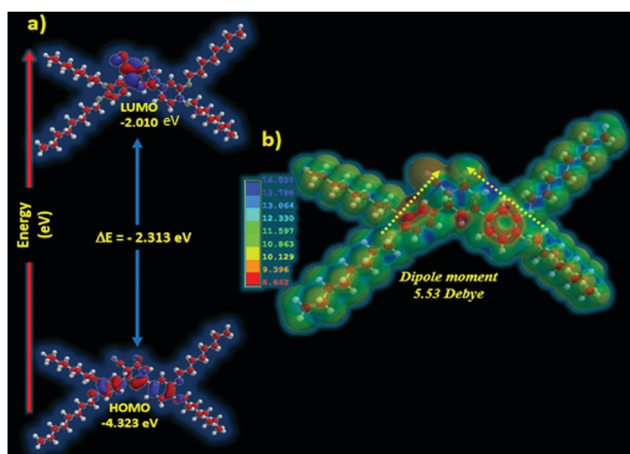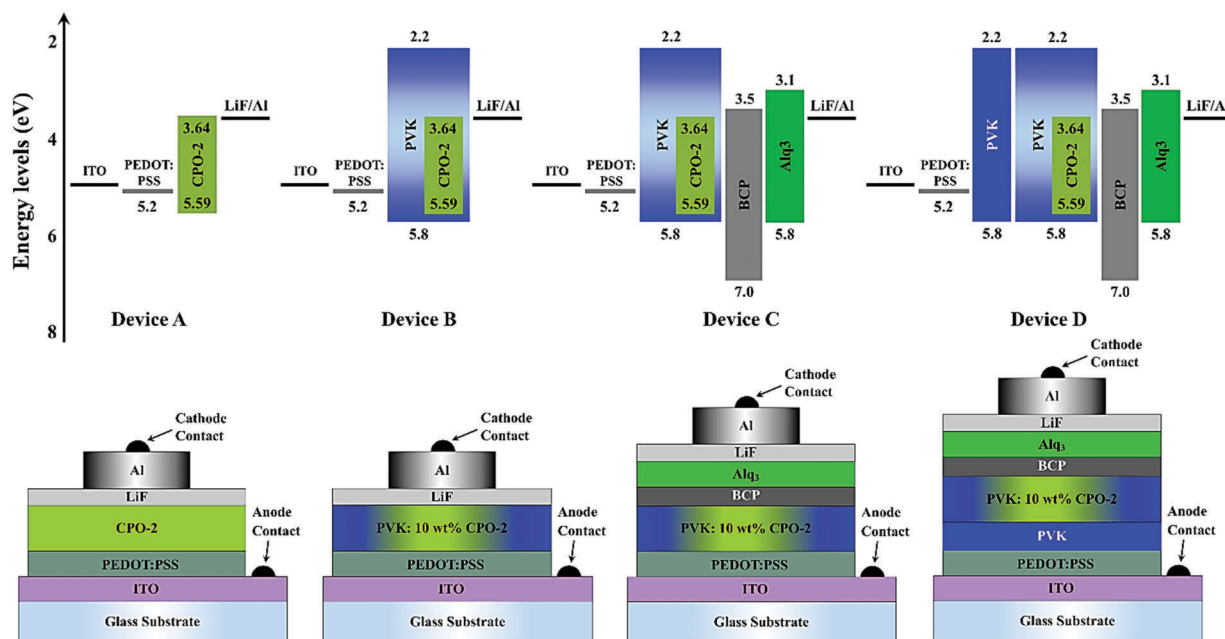
Fig. 13 Energy-level diagram of the materials used and schematic of different OLED architectures.

Table 6 Electroluminescence performance data of OLEDs

Device	V_{onset}[e] (V)	L_{max}[f] (cd m^{-2})	η_c[g] (cd A^{-1})	η_p[g] (lm W^{-1})	η_{EQE}[g] (%)
A[ah]	11.0	—	—	—	—
B[b]	7.12	261	0.33	0.09	0.14
C[c]	6.41	673	0.86	0.26	0.51
D[d]	5.69	1055	1.06	0.35	0.69

[a] Device configuration: ITO (120 nm)/PEDOT:PSS (50 nm)/CPO-2 (80 nm)/LiF (1 nm)/Al (150 nm). [b] Device configuration: ITO (120 nm)/PEDOT:PSS (50 nm)/PVK:10 wt% **CPO-2** (80 nm)/LiF (1 nm)/Al (150 nm). [c] Device configuration: ITO (120 nm)/PEDOT:PSS (50 nm)/PVK:10 wt% **CPO-2** (80 nm)/BCP (6 nm)/Alq$_3$ (35 nm)/LiF (1 nm)/Al (150 nm). [d] Device configuration: ITO (120 nm)/PEDOT:PSS (50 nm)/PVK (40 nm)/PVK:10 wt% **CPO-2** (80 nm)/BCP (6 nm)/Alq$_3$ (35 nm)/LiF (1 nm)/Al (150 nm). [e] V_{onset}: turn-on voltage at a luminance of 1 cd m^{-2}. [f] L_{max}: luminance at 20 V. [g] Current efficiency (η_c), power efficiency (η_p) and external quantum efficiency (η_{EQE}) at 100 cd m^{-2}. [h] Very weak emission was observed.

drive voltage (V_{onset} corresponding to 1 cd m^{-2}) of 7.12 V, a low luminance (L_{max}) of 261 cd m^{-2}, a current efficiency (η_c) of 0.33 cd A^{-1}, a power efficiency (η_p) of 0.09 lm W^{-1} and an external quantum efficiency (η_{EQE}) of 0.14% at 100 cd m^{-2}. Here, the high drive voltage indicates the presence of high charge injection barriers in the device. On the other hand, a significant improvement in the device performance (L_{max} of 673 cd m^{-2}, η_c of 0.86 cd A^{-1}, η_p of 0.26 lm W^{-1} and η_{EQE} of 0.14%) was noticed with PVK: **CPO-2** (10 wt%) as the emitting material (device C) together with bathocuproine (BCP) and tris-(8-hydroxyquinoline)-aluminum (Alq$_3$) as the hole blocking material and the electron transport material, respectively. In addition, the device exhibited a relatively low V_{onset} of 6.41 V. We can ascribe the improvement in the performance of the device C to the efficient transfer of exciton energy to the emissive dopant from the host material and/or a balanced injection of charge carriers (hole/electron) into the emitter layer.[47,48] Here BCP confines the reductant holes in the emitting layer that did not recombine with the electrons in the emitting zone.[49] Further improvement in the performance of the device was noticed for device D with PVK as a hole transport material which showed better efficiencies of η_c: 1.06 cd A^{-1}, η_p: 0.35 lm W^{-1}, η_{EQE}: 0.69% and L_{max} of 1055 cd m^{-2} than that of device C. Here, V_{onset} was further reduced to 5.69 V. All the OLEDs under investigation emitted in the yellowish green region when ITO was positively biased. The steady-state electroluminescence (EL) spectra (Fig. 14b) of the OLEDs operating at the 20 V showed emission peaks at ∼560 nm with a full-width half maxima of ∼89 nm. It can be noted that the EL spectra and the thin film fluorescence spectra of **CPO-2** (Fig. 14b) are almost the same, indicating that both originate from the same excited state. Fig. 14c shows that there is no change in the shape and peak of the EL spectra, demonstrating that the devices possess excellent spectral stability. The CIE chromaticity coordinates (0.425, 0.553) corresponding to bright green emission were determined using the EL spectra of the OLEDs at 15 V. Fig. 14d depicts the chromaticity diagram of the OLEDs. It is worth mentioning that the investigated OLEDs are unoptimized. The device performance can be improved by further optimization. These observations offer the potential use of **CPO-2** in OLED applications with an additional scope to improve with slight modifications in the molecular design and device architecture.

Conclusions

A new series of flying bird shaped D–A–D configured cyanopyridone-based molecules (**CPO-1** to **CPO-4**) carrying different alkoxy chains were rationally designed and synthesized. Their meso-morphic, photophysical, electrochemical and electrolumines-cence properties have been explored. The results reveal that
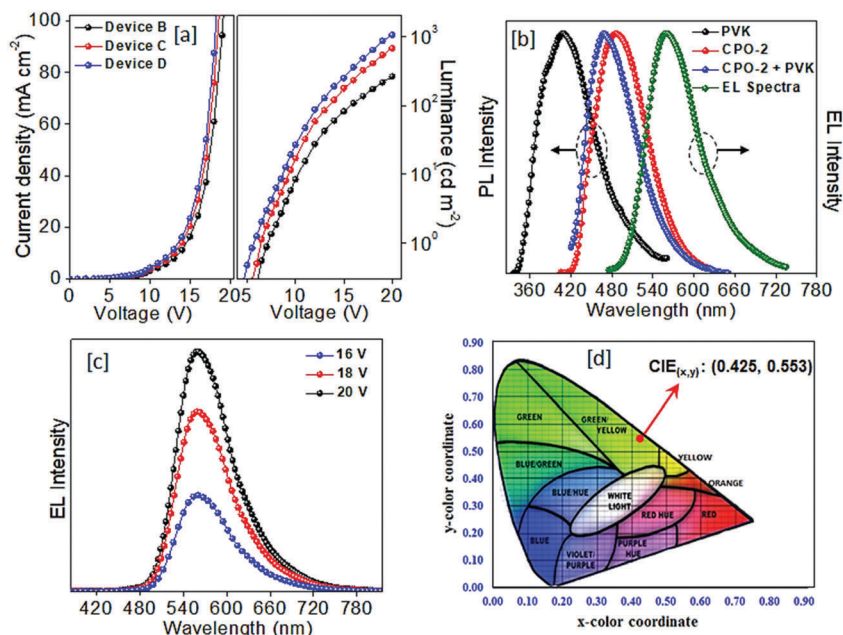
Fig. 14 (a) $J-V-L$ characteristics; (b) PL spectra of PVK, CPO-2, PVK:10 wt% CPO-2 thin films and EL spectra of device D; (c) EL spectra of device D at different bias voltages and (d) chromaticity diagram of the OLEDs.

they display thermotropic mesophase behavior by means of self-assembly of more or less disc-shaped H-bonded dimers. Furthermore, the role of H-bonding interactions in the stabilization of mesophases was determined by the support of one more similar series of molecules (**MCP-1** to **MCP-3**). They adopted various columnar mesophases depending on the dynamics of the H-bonded dimeric entities in the columnar stack as well as the length of the terminal alkyl chains. Mesogens emit bright greenish blue light in the range of 478–486 nm mainly due to their effective intramolecular charge transport ability, which was further evidenced by theoretical simulations. In the fabricated OLEDs using **CPO-2** as an emitter, the host–guest configured devices showed encouraging results. Evidently, the promising device efficiency offers a new designing strategy to achieve efficient emitting LCs for OLED applications. It is expected that by appropriate tailoring of the donors attached to the cyanopyridone core, it would be possible to improve the quantum yield of the materials and hence further enhance the device efficiency.

Conflicts of interest

There are no conflicts of interest to declare.

Acknowledgements

References

1 M. O'Neill and S. M. Kelly, *Adv. Mater.*, 2003, **15**, 1135–1146.

2 S. Laschat, A. Baro, N. Steinke, F. Giesselmann, C. Haegele, G. Scalia, R. Judele, E. Kapatsina, S. Sauer and A. Schreivogel, *Angew. Chem., Int. Ed.*, 2007, **46**, 4832–4887.

3 B. R. Kaafarani, *Chem. Mater.*, 2010, **23**, 378–396.

4 S. Kumar, *Chemistry of discotic liquid crystals: form monomers to polymers*, Taylor and Francis, CRC Press, Boca Raton (FL), 2011.

5 Y. Wang, J. Shi, J. Chen, W. Zhu and E. Baranoff, *J. Mater. Chem. C*, 2015, **3**, 7993–8005.

6 R. K. Gupta, D. Das, M. Gupta, S. K. Pal, P. K. Iyer and A. S. Achalkumar, *J. Mater. Chem. C*, 2017, **5**, 1767–1781.

7 A. P. Sivadas, D. S. Rao, N. S. Kumar, D. D. Prabhu, S. Varghese, C. N. Ramachandran, R. M. Ongungal, S. Krishna Prasad and S. Das, *J. Phys. Chem. B*, 2017, **121**, 1922–1929.

8 Y. Wang, Y. Liao, C. P. Cabry, D. Zhou, G. Xie, Z. Qu, D. W. Bruce and W. Zhu, *J. Mater. Chem. C*, 2017, **5**, 3999–4008.

9 A. K. Yadav, B. Pradhan, H. Ulla, S. Nath, J. De, S. K. Pal, M. N. Satyanarayan and A. S. Achalkumar, *J. Mater. Chem. C*, 2017, **5**, 9345–9358.

10 Y. Kamikawa, M. Nishii and T. Kato, *Chem. – Eur. J.*, 2004, **10**, 5942–5951.

11 K. E. Maly, C. Dauphin and J. D. Wuest, *J. Mater. Chem.*, 2006, **16**, 4695–4700.

12 T. Kato, N. Mizoshita and K. Kishimoto, *Angew. Chem., Int. Ed.*, 2006, **45**, 38–68.

13 K. Kanie, T. Yasuda, S. Ujiie and T. Kato, *Chem. Commun.*, 2000, 1899–1900.

14 K. Kanie, T. Yasuda, M. Nishii, S. Ujiie and T. Kato, *Chem. Lett.*, 2001, 480–481.

15 K. Kanie, M. Nishii, T. Yasuda, T. Taki, S. Ujiie and T. Kato, *J. Mater. Chem.*, 2001, **11**, 2875–2886.

16 R. Kleppinger, C. P. Lillya and C. Yang, *Angew. Chem., Int. Ed. Engl.*, 1995, **34**, 1637–1638.

17 M. Suarez, J.-M. Lehn, S. C. Zimmerman, A. Skoulios and B. Heinrich, *J. Am. Chem. Soc.*, 1998, **120**, 9526–9532.

18 J. K. Hirschberg, L. Brunsveld, A. Ramzi, J. A. Vekemans, R. P. Sijbesma and E. W. Meijer, *Nature*, 2000, **407**, 167.

19 E. Beltrán, E. Cavero, J. Barberá, J. L. Serrano, A. Elduque and R. Giménez, *Chem. – Eur. J.*, 2009, **15**, 9017–9023.

20 X. Zhu, A. Mourran, U. Beginn, M. Möller, D. V. Anokhin and D. A. Ivanov, *Phys. Chem. Chem. Phys.*, 2010, **12**, 1444–1452.

21 H. Blanco, V. Iguarbe, J. Barberá, J. L. Serrano, A. Elduque and R. Giménez, *Chem. – Eur. J.*, 2016, **22**, 4924–4930.

22 P. Fuchs, C. Tschierske, K. Raith, K. Das and S. Diele, *Angew. Chem.*, 2002, **114**, 650–653.

23 S. Yagai, Y. Goto, T. Karatsu, A. Kitamura and Y. Kikkawa, *Chem. – Eur. J.*, 2011, **17**, 13657–13660.

24 S. Yagai, Y. Goto, X. Lin, T. Karatsu, A. Kitamura, D. Kuzuhara, H. Yamada, Y. Kikkawa, A. Saeki and S. Seki, *Angew. Chem.*, 2012, **124**, 6747–6751.

25 C. Tschierske, *Angew. Chem., Int. Ed.*, 2013, **52**, 8828–8878.

26 T. Kato, T. Yasuda, Y. Kamikawa and M. Yoshio, *Chem. Commun.*, 2009, 729–739.

27 T. Wöhrle, I. Wurzbach, J. Kirres, A. Kostidou, N. Kapernaum, J. Litterscheidt, J. C. Haenle, P. Staffeld, A. Baro and F. Giesselmann, *Chem. Rev.*, 2015, **116**, 1139–1241.

28 A. H. Abadi, T. M. Ibrahim, K. M. Abouzid, J. Lehmann, H. N. Tinsley, B. D. Gary and G. A. Piazza, *Bioorg. Med. Chem.*, 2009, **17**, 5974–5982.

29 O. V. Ershov, S. V. Fedoseev, M. Y. Ievlev and M. Y. Belikov, *Dyes Pigm.*, 2016, **134**, 459–464.

30 M. Hagimori, Y. Shigemitsu, R. Murakami, K. Yokota, Y. Nishimura, N. Mizuyama, B.-C. Wang, C.-K. Tai, S.-L. Wang and T.-L. Shih, *Dyes Pigm.*, 2016, **124**, 196–202.

31 D. Z. Mijin, M. Baghbanzadeh, C. Reidlinger and C. O. Kappe, *Dyes Pigm.*, 2010, **85**, 73–78.

32 J. Mirković, J. Lović, M. A. Ivić and D. Mijin, *Electrochim. Acta*, 2014, **137**, 705–713.

33 R. Kleppinger, C. P. Lillya and C. Yang, *J. Am. Chem. Soc.*, 1997, **119**, 4097–4102.

34 T. N. Ahipa and A. V. Adhikari, *Tetrahedron Lett.*, 2014, **55**, 495–500.

35 T. N. Ahipa, V. Kumar, D. S. Rao, S. K. Prasad and A. V. Adhikari, *CrystEngComm*, 2014, **16**, 5573–5582.

36 T. N. Ahipa and A. V. Adhikari, *Photochem. Photobiol. Sci.*, 2014, **13**, 1496–1508.

37 T. N. Ahipa and A. V. Adhikari, *New J. Chem.*, 2014, **38**, 5018–5029.

38 Q. Zhang, H. Peng, G. Zhang, Q. Lu, J. Chang, Y. Dong, X. Shi and J. Wei, *J. Am. Chem. Soc.*, 2014, **136**, 5057–5064.

39 Z. Wang, Y. Lan, K. Zhong, Y. Liang, T. Chen and L. Y. Jin, *Int. J. Mol. Sci.*, 2014, **15**, 5634–5648.

40 B.-K. Cho and S.-H. Kim, *Soft Matter*, 2014, **10**, 553–559.

41 J. Tang, R. Huang, H. Gao, X. Cheng, M. Prehm and C. Tschierske, *RSC Adv.*, 2012, **2**, 2842–2847.

42 S. Park and B.-K. Cho, *Soft Matter*, 2015, **11**, 94–101.

43 S. Moyano, J. Barberá, B. E. Diosdado, J. L. Serrano, A. Elduque and R. Giménez, *J. Mater. Chem. C*, 2013, **1**, 3119–3128.

44 G. A. Crosby and J. N. Demas, *J. Phys. Chem.*, 1971, **75**, 991–1024.

45 A. M. Brouwer, *Pure Appl. Chem.*, 2011, **83**, 2213–2228.

46 S. K. Pal, I. Bala, S. P. Gupta and J. De, *Chem. – Eur. J.*, 2017, **23**, 12767–12778.

47 H. Ulla, M. R. Kiran, B. Garudachari, T. N. Ahipa, K. Tarafder, A. V. Adhikari, G. Umesh and M. N. Satyanarayan, *J. Mol. Struct.*, 2017, **1143**, 344–354.

48 H. Ulla, M. Raveendra Kiran, B. Garudachari, M. N. Satyanarayan, G. Umesh and A. M. Isloor, *Opt. Mater.*, 2014, **37**, 311–321.

49 S. Chidirala, H. Ulla, A. Valaboju, M. R. Kiran, M. E. Mohanty, M. N. Satyanarayan, G. Umesh, K. Bhanuprakash and V. J. Rao, *J. Org. Chem.*, 2016, **81**, 603–614.

This journal is © The Royal Society of Chemistry 2018

J. Mater. Chem. C, 2018, **6**, 7385–7399 | 7399